Energy Conversion and Management: X 20 (2023) 100444

Contents lists available at ScienceDirect

Energy Conversion and Management: X

journal homepage: www.sciencedirect.com/journal/energy-conversion-and-management-x

CPFD simulation of an electrically heated fluidized bed calciner with binary particles

Ron M. Jacob *, Lars-André Tokheim

University of South-Eastern Norway, Kjølnes Ring 56, 3918 Porsgrunn, Norway

ARTICLE INFO

Keywords:
Electrified calciner
Fluidized bed
CO_2 capture
Calcination kinetics
Heat transfer

ABSTRACT

Electrifying a calciner with clean energy can cut fuel emissions and produce a stream of relatively pure CO_2 from the calcination reaction ($CaCO_3 \rightarrow CaO + CO_2$), which can be utilized or stored. A fluidized bed calciner offers a high heat transfer coefficient and requires low gas flow rates for operation. The design of such a reactor is studied in this work. It is not possible to fluidize raw meal directly, so a binary mixture of coarse lime particles and fine raw meal is used. The commercial Barracuda CPFD software is applied. The model was first validated against experimental results and then used to find an optimized design. The results indicate that the suggested pilot-scale fluidized bed calciner can operate between 10 and 16 t/h of raw meal feeding with a calcination degree above 90% and with negligible coarse particle entrainment. The calciner needs 0.05–0.09 kg-CO_2/kg-raw-meal for the operation, so the required gas recycling is low. Overall the calciner operation is smooth, and such a design could be used for electrification combined with CCUS.

Introduction

The cement industry emitted around 2.5 Gt of CO_2 in 2021, making it the second largest emitter in the industrial sector [1]. Without emission abatement steps, this number is expected to rise as the cement demand will most likely increase by 12–13 % in 2050 [2]. Despite improving energy efficiency and using alternative fuels, the emissions are high due to the CO_2 generated from the decomposition of calcite (i.e., $CaCO_3 \rightarrow CaO + CO_2$), which is the key ingredient. The CO_2 generated from calcite decomposition accounts for around two-thirds of the emissions [2]. Around 94% of the calcite decomposition happens inside the cement calciner. The calcite decomposition consumes about 1.7 MJ/kg$CaCO_3$ [3], so the calciner is the most energy-intensive equipment in the cement industry.

Today, cement calciners are usually based on the entrained flow concept wherein the flue gases from the combustion entrain the particles through the reactor [4], while heat is transferred to the solids by direct contact with the hot combustion gases. The flue gas is a mixture of gases such as N_2, CO_2, NO_x, SO_x, and CO_2 can be captured from the flue gas for utilization or storage (CCUS).

Post-combustion capture technologies, such as amine based CO_2 extraction, could be used to reduce CO_2 emissions [5]. However, such a technology is energy-intensive, as regeneration of standard amine solutions consumes around 3.7 MJ/kg-CO_2 [6]. Alternatively, oxy-fuel technology could be employed [7]. In this technology, a high concentration of CO_2 can be produced by burning a carbon-rich fuel with pure oxygen instead of air. Despite the energy penalty related to the air separation unit (ASU), the oxy-fuel combustion consumes less energy than amine-based capture. Implementing this technology in the cement industry will however affect all the equipment in the kiln system and therefore lead to a high capital cost [8]. Another alternative is the indirectly heated calcium looping (IHCaL) technology [9,10]. IHCaL utilizes a calcium based sorbent (limestone), which circulates between a carbonator and a calciner. The sorbent captures the CO_2 in the carbonator, and this captured CO_2 is then released in the calciner. The IHCaL concept indirectly heats the calciner through sodium filled heat pipes which get its energy from an external combustor [9]. Indirect heating of the calciner produces a relatively pure CO_2 from limestone decomposition, and this CO_2 can be further processed for utilization or storage. Alternatively, the calciner in cement clinker production could be externally heated to directly capture CO_2 released from the raw material (mainly limestone) [8]. This concept of direct capture is being studied in the Low Emissions Intensity Lime And Cement (LEILAC) project [11,12], which uses an externally heated long vertical tube as a calciner (drop tube calciner). The raw meal is fed from the top of this tube, and the heated tube provides energy for heating and calcite decomposition while

* Corresponding author at: Borgehaven 23, Porsgrunn 3911, Norway.
E-mail addresses: Ron.Jacob@usn.no (R.M. Jacob), Lars.A.Tokheim@usn.no (L.-A. Tokheim).

https://doi.org/10.1016/j.ecmx.2023.100444
Received 8 June 2023; Received in revised form 9 August 2023; Accepted 19 August 2023
Available online 21 August 2023

the meal drops down due to gravity.

As the share of renewables increases in electricity production, the cement calciner could preferably be heated by electrical energy instead of fuel combustion. Electrical heating will act like a direct capture technology to produce relatively pure CO_2 from the calcite decomposition step. A study indicates that this technology may be cost-competitive against the post-capture technology of amine scrubbing [13]. Compared to a system with a coal-fired calciner, the emissions from the kiln system could be reduced by 78% by electrifying just the calciner [14].

The entrained flow calciner, the reactor concept used in the industry today, may be challenging to electrify as it requires a lot of gas recycling to compensate for the absence of flue gases from the combustion process [15]. This can increase the duty of the calciner by 20% compared to calciner designs with no recycling, as the sensible heat loss from the gas exiting the calciner increases [14]. Designs such as the drop tube calciner [11,12] and the rotary calciner [16] may instead be used, as these technologies do not require any gas to be recycled. However, the heat transfer in these systems may not be very efficient and therefore a huge heat transfer area is required. This means that the system will increase in size and have a larger surface area, which will increase the losses from the external calciner surface through convection and radiation. The electrified fluidized bed calciner technology may offer a solution here as it has a high heat transfer due to good bed mixing [17,18]. So, the surface heat loss will be minimized. Further, the operation velocities are low, requiring low gas recycling. Thus, the sensible heat loss from the gas exiting from the system is also low [14]. Hence, this technology seems to be a promising option for electrified calcination combined with CCUS.

The raw meal (raw material mixture heated to produce clinker) is a cohesive powder and hard to fluidize, as the particles belong to the Geldart C [19] category in the classification system developed by Geldart [20]. However, it may be possible to fluidize Geldart C particles by mixing them with Geldart B particles, which are easily fluidized [19]. By operating at an appropriate velocity, the Geldart C particles could simultaneously be segregated from the Geldart B particles in the bed. This technology was demonstrated by Kato et al. by fluidizing fine limestone particles in a calciner called a Powder Particle Fluidized Bed [21]. Tashimo et al. [22] conducted several tests with limestone of 2 – 64 μm mixed with coarse sand of 420 – 840 μm to demonstrate the calcination of limestone with this technology.

Even though Tashimo et al. [22] demonstrated the fluidized bed calciner technology operating with binary particles, the feeding rate of fine particles was extremely low compared to the gas required from the bottom. This means that a full-scale system requires high gas recycling, which could lead to high sensible heat loss, as demonstrated in a previous article [14]. Tashimo et al. [22] used only the gas from the bottom to entrain the fine particles from the system. However, the calcination reaction also produces CO_2 gas as high as 0.44 $kgCO_2/kgCaCO_3$, according to stochiometric balance. The CO_2 production could be increased by increasing the feeding rate of fine particles (containing calcite), which could be used to entrain fine particles. This will significantly reduce the gas required from the bottom of the bed. Furthermore, to minimize changes in the product's chemical composition, in cases where perfect separation of coarse and fine particles is not possible, lime (calcined limestone) particles may be used as the coarse fraction in the mixture.

This study aims to demonstrate a fluidized bed calciner design operating with binary particles, potentially requiring a lower gas from the bottom than previously demonstrated by Tashimo et. al. [22]. The design is studied by means of computational particle fluid dynamics (CPFD) simulations. The commercial Barracuda ver 22.1.0 CPFD software is utilized for simulations.

To fulfill the main aim, the objectives of the study are to 1) establish a CPFD model of a fluidized bed calciner, 2) validate the model with experimental results, 3) utilize the validated model to simulate the calciner operating with a raw meal feeding between 10 and 24 t/h. This feed rate is about 10% of that in a full-scale system. Hence, the present study is relevant for a pilot-scale system, which may later be up-scaled to a full-scale industrial system.

Methods

Calciner description

The design and dimension of the fluidized bed calciner operating with binary particles are shown in Fig. 2.1. The fluidized bed calciner is designed to handle a binary mixture of raw meal and coarse lime, as it is not possible to fluidize raw meal alone. The coarse particles are assumed to be lime, so even if some of this is eroded in the bed, the effect will be less pronounced downstream as the calcined raw meal mainly consists of lime. The design features two chambers, and the binary mixture is fluidized with CO_2.

The first chamber is at the bottom and is called the mixing chamber as its main role is to mix the fine raw meal with the coarse heated particles in the bed, and thereby provide efficient heat transfer to the meal. The mixing chamber is heated by heating elements placed inside the vertical sections. The particle mostly flows parallel to the vertical sections, so the erosion risk is lower when compared to inserted horizontal heating rods (an alternative configuration not studied in this article). The raw meal enters the mixing chamber from three locations, gets fluidized by the fluidized coarse lime particles, and gets enough energy to be heated and calcined while being in contact with the inert phase. Several feeding locations improve the meal distribution across the bed, thus improving the heat transfer.

The calcination process releases CO_2, which entrains the particles to the second chamber, which is called the segregation chamber. The segregation chamber is designed to entrain the calcined raw meal but not the coarse particles; they will remain in the bed. If some coarse particles are entrained, they could be replenished by feeding a make-up stream along with the raw meal. The calcined raw meal exits from the outlet end, i.e., at the top of the calciner.

The designed calciner is evaluated with CPFD simulations, as described in subsequent sections. The properties of particles used in simulations are shown in Fig. 2.2. The raw meal's composition and particle size distribution (PSD) is taken from experimental work and used in the simulations. The PSD of coarse lime is assumed to have a normal distribution with a mean of 600 μm and a standard deviation of 50 μm. Pure CO_2 is fed from the bottom of the calciner for fluidization.

CPFD method

CPFD is a method to simulate multiphase solid–gas flow. The commercial CPFD software Barracuda ver 22.1.0 was used in this work. CPFD uses a unique multiphase-particle-in-cell (MP-PIC) method where the fluid phase is solved in the Eulerian cell. In contrast, the particle phase is solved both in the Eulerian cell and as Lagrangian particles [23,24]. The particles in the Lagrangian phase are represented by numerical particles (or parcels), where each parcel represents several physical particles of similar size, velocity, and position [23,24]. As particles with the same characteristics will likely behave similarly in the reactor, it is not necessary to compute the behavior of every physical particle. Instead, a statistically significant number of numerical particles is applied to represent the physical particles. Computationally intensive properties such as particle stresses are more efficiently calculated in Eulerian cells because there are fewer Eulerian cells than particle parcels [23]. This method can efficiently handle a range of particle phases from dilute to dense, different PSDs, and different particle materials.

Governing equations

The volume-averaged continuity and momentum equation for the fluid phase are shown in Eqs. (1) and (2) [25]. Here, $\dot{m}_{f,g}$ is the mass

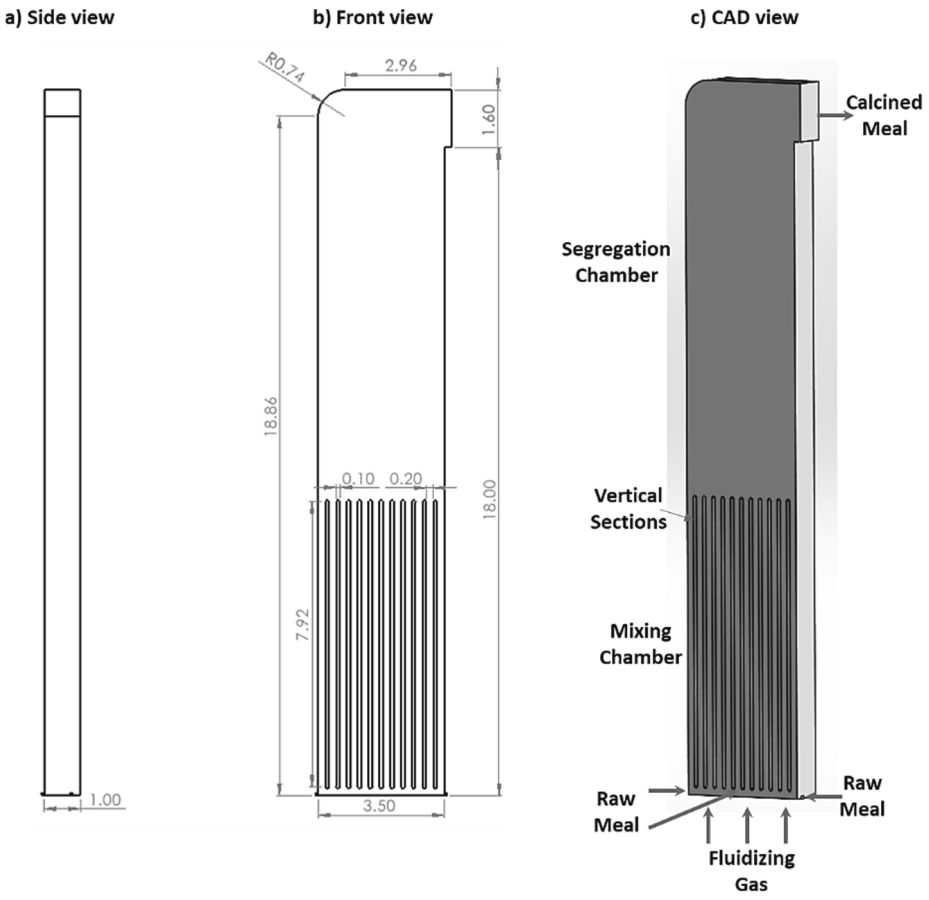

Fig. 2.1. Design and dimensions (m) of the fluidized bed calciner studied in this work.

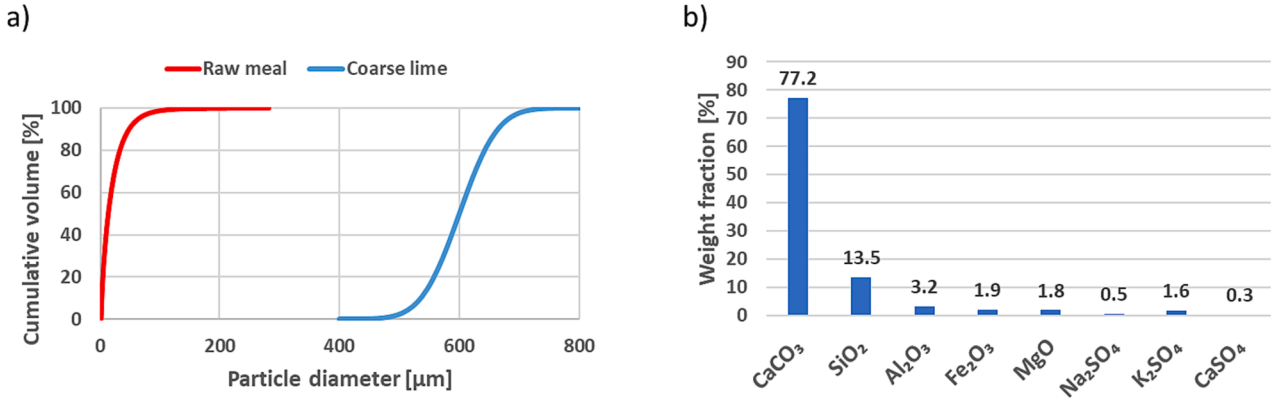

Fig. 2.2. Particle characteristics with a) PSD of raw meal and coarse lime particles, b) raw meal composition.

generation rate of fluid per volume due to particle–fluid chemical reactions, θ_f, u_f and ρ_f are the volume fraction, velocity, and density of the fluid, respectively. The CPFD model uses the ideal gas law to compute the gas density. ∇p is the pressure gradient across flowing gas, τ_f is the fluid stress tensor, g is the acceleration due to gravity, and F is the momentum exchange rate from gas to particle per unit volume, which will be discussed later in this section.

$$\frac{\partial(\theta_f\rho_f)}{\partial t}+\nabla\bullet\left(\theta_f u_f\rho_f\right)=\dot{m}_{f,g} \tag{1}$$

$$\frac{\partial(\theta_f u_f\rho_f)}{\partial t}+\nabla\bullet\left(\theta_f\rho_f u_f u_f\right)=-\nabla p-F+\theta_f\rho_f g+\nabla\bullet\left(\theta_f\tau_f\right) \tag{2}$$

The fluid stress tensor (τ_f) is given by Eq. (3) [25]. Here, μ is the fluid viscosity which is the sum of laminar shear viscosity (taken from [26]) and turbulence viscosity (μ_t). The CPFD model uses the turbulence model of large eddy simulations (LES). In the LES model, large eddies are directly resolved, while the eddies smaller than the mesh are modelled with the turbulence viscosity (μ_t) given by Eq. (4), based on Smagorinsky's model [27]. Here Δ is the sub-grid length scale (assumed to be given by Eq. (5) [25] where dx, dy, and dz represents each cell size in the computational domain), and C is model constant (assumed to be 0.01 [25]).

$$\tau_f=\mu\left(\frac{\partial u_{f,i}}{\partial x_j}-\frac{\partial u_{f,j}}{\partial x_i}\right)-\frac{2}{3}\delta_{i,j}\mu\frac{\partial u_k}{\partial x_k} \tag{3}$$

$$\mu_t = C\rho_f \Delta^2 \sqrt{\left(\frac{\partial u_{f,i}}{\partial x_j} - \frac{\partial u_{f,j}}{\partial x_i}\right)^2} \tag{4}$$

$$\Delta = \sqrt[3]{sum(dxdydz)} \tag{5}$$

The transport equation is solved separately for each gas species based on their mass fraction ($Y_{f,i}$) and this is given by Eq. (6) [25]. Here, D_t is the turbulent mass diffusivity, which is related to the turbulent Schmidt number (Sc_t, with a standard value of 0.9 [25]) by Eq. (7) and $\dot{m}_{i,chem}$ represents the mass transferred between gas species due to chemical reactions.

$$\frac{\partial(\theta_f \rho_f Y_{f,i})}{\partial t} + \nabla \bullet (\theta_f u_f \rho_f Y_{f,i}) = \nabla \bullet (\rho_f D_t \theta_f \nabla Y_{f,i}) + \dot{m}_{i,chem} \tag{6}$$

$$\frac{\mu_t}{\rho_f D_t} = Sc_t \tag{7}$$

The energy balance of the fluid phase is then given by Eq. (8) [25]. Enthalpy (H_f) and specific heat capacity ($C_{p,f}$) of the fluid mixture are taken from previous work [14]. ϕ is the viscous dissipation term, $\dot{Q}$ is the energy source and S_h is the energy exchange from particles to fluid phase. $\dot{q}_f^{''}$ in fluid heat flux and this is given by Eq. (9). Further T_f is the temperature of fluid, k_f is the sum of molecular conductivity (taken from [26]), and eddy conductivity ($k_{f,t}$) which is related to turbulent Prandtl number (Pr_t, with standard value of 0.9 [25]) given by Eq. (10). $\dot{q}_D$ is the enthalpy diffusion term and this is given by Eq. (11) [25].

$$\frac{\partial(\theta_f \rho_f H_f)}{\partial t} + \nabla \bullet (\theta_f \rho_f H_f u_f) = \theta_f \left(\frac{\partial p}{\partial t} + u_f \nabla p\right) + \phi - \nabla \bullet (\theta_f q_f^{''}) + \dot{Q} + S_h + \dot{q}_D + \dot{q}_w \tag{8}$$

$$\dot{q}_f^{''} = -k_f \nabla T_f \tag{9}$$

$$\frac{\mu_t C_{p,f}}{k_{f,t}} = Pr_t \tag{10}$$

$$\dot{q}_D = \sum_{i=1}^{N} \nabla \bullet (H_{f,i} \theta_f \rho_f D_t \nabla Y_{f,i}) \tag{11}$$

The momentum exchange from fluid to particles (F) and energy exchange from particles to gas (S_h) are given by Eqs. (12) and (13) [25]. These terms connect the momentum and energy balance between the fluid and particles phase. Here, H_p and $C_{p,p}$ are the enthalpy and specific heat capacity of the particles, which are taken from previous work [14]. The change in mass of particles per time (i.e. dm_p/dt) depends on chemical kinetics which will be described in a later section. D is the drag function which is also discussed in a later section.

$$F = \iiint f \left\{ m_p \left[D(u_f - u_p) - \frac{1}{\rho_p} \nabla p \right] \right\} dm_p du_p dT_p \tag{12}$$

$$S_h = \iiint f \left\{ m_p \left[D(u_p - u_f)^2 - C_{p,p} \frac{dT_p}{dt} \right] - \frac{dm_p}{dt} \left[H_p + \frac{1}{2}(u_p - u_f)^2 \right] \right\} dm_p du_p dT_p \tag{13}$$

f in Eq. (12) is the particle distribution function which is a function of particle mass (m_p), particle density (ρ_p), particle velocity (u_p), particle temperature (T_p), spacial position (x_i), and time (t) [23,25]. The evolution of f is governed by the Liouville equation given by Eq. (14) [23]. The Eulerian equation for particles is then given by taking moments of Eq. (14) and multiplying it by m_p and $m_p u_p$ [23].

$$\frac{\partial f}{\partial t} + \nabla \bullet (f u_p) + \nabla \bullet (f A_{p,bd}) = 0 \tag{14}$$

The energy balance of the particles is given by Eq. (15) by assuming a lumped-heat Eq. [25]. Here, A_{sp} is the surface area of particles and h_p is the heat transfer coefficient between the fluid and the particles, and this is further discussed in a later section.

$$m_p C_{p,p} \frac{dT_p}{dt} = h_p A_{sp} (T_f - T_p) \tag{15}$$

The acceleration of the particles is modelled with a Blended Acceleration Model (BAM) and is given by Eq. (16) [28]. Here, θ_p is the particle volume fraction, and $g_1(\theta_p)$ is the blending function which is a function of particle volume fraction [28]. The relative motion between particles of different sizes and densities is lower than that between particles of the same size and density [28]. This factor becomes more important with a denser packing of particles. So, BAM has separate acceleration terms at close-pack conditions ($A_{p,cp}$) and at dilute packing of particles (A_p) and these are given by Eqs. (17) and (18) [28]. As the packing of particles increases (or θ_p increases), $A_{p,cp}$ becomes more important, while A_p becomes important at low packing conditions (or θ_p low). At close pack conditions, all the particles are assumed to have the same averaged drag function ($\overline{D}$) and drag-averaged particle velocity ($\widetilde{u_p}$) which can be found in literature [28].

$$A_{p,bd} = g_1(\theta_p) A_{p,cp} + [1 - g_1(\theta_p)] A_p \tag{16}$$

$$A_p = \frac{\partial u_p}{\partial t} = D(u_f - u_p) - \frac{1}{\rho_p} \nabla p + g - \frac{1}{\theta_p \rho_p} \nabla \tau_p \tag{17}$$

$$A_{p,cp} = \overline{D}(u_f - \widetilde{u_p}) - \frac{1}{\rho_p} \nabla p + g - \frac{1}{\theta_p \rho_p} \nabla \tau_p \tag{18}$$

The particle–particle interactions are modelled with particle normal stress (τ_p) given by Eq. (19) [24]. Here, ε is a small number to avoid numerical error when the particle volume fraction (θ_p) in any Eulerian cell becomes equal to its maximum packing given by close pack conditions (θ_{cp}). The parameters P_s and β are chosen to be 1 and 3 based on recommended values [29].

$$\tau_p = \frac{P_s \theta_p^{\beta}}{max[\theta_{cp} - \theta_p, \varepsilon(1 - \theta_p)]} \tag{19}$$

Drag model

The interphase drag function (D) is used to couple particle and fluid phases, and several models, including the Ergun and Wen-Yu drag models, could be used in simulations. The Ergun drag model was developed for dense phase regions, given by Eq. (20) [30]. Here, the Reynolds number (Re) is given by Eq. (21). The recommended values of 2 and 180 are used for the model coefficients c_o and c_1 [29], respectively.

$$D = \left(\frac{c_1 \theta_p}{\theta_f Re} + c_o\right) \frac{\rho_f (u_f - u_p)}{d_p \rho_p} \tag{20}$$

$$Re = \frac{d_p \rho_f |u_f - u_p|}{\mu} \tag{21}$$

The Wen-Yu model [31] was developed for single particles and then modified to include the dependence on the fluid void fraction (θ_f). The drag coefficient (C_d) based on the Wen-Yu model is given by Eq. (22), and the interphase drag function (D) is related to the drag coefficient (C_d) by Eqs. (23) [29]. The recommended values of 1, 0.15, 0.44, −2.65, and 0.687 are used for the model coefficient c_o, c_1, c_2, n_o, and n_1 respectively [29].

$$C_d = \begin{cases} \frac{24}{Re}\theta_f^{n_o} Re < 0.5 \\ \frac{24}{Re}\theta_f^{n_o}(c_o + c_1 Re^{n_1}) 0.5 \le Re \le 1000 \\ c_2 \theta_f^{n_o} Re > 1000 \end{cases} \quad (22)$$

$$D = \frac{3}{8} C_d \frac{\rho_f (u_f - u_p)}{r_p \rho_p} \quad (23)$$

The Wen-Yu drag model is more appropriate for dilute flows, while the Ergun drag model is more appropriate for dense flows. Using a blend of the two may capture the best of both drag models. The blended drag function (D) is given by Eq. (24). Here, D_1 is the drag function from the Wen-Yu equation and D_2 is the drag function from the Ergun equation.

$$D = \begin{cases} D_1 \theta_p < 0.75\theta_{CP} \\ \frac{(D_2 - D_1)(\theta_p - 0.75\theta_{cp})}{0.85\theta_{cp} - 0.75\theta_{cp}} + D_1 0.75\theta_{cp} \le \theta_p \le 0.85\theta_{cp} \\ D_2 \theta_p > 0.85\theta_{CP} \end{cases} \quad (24)$$

Heat transfer

The heat transfer coefficient between the particles and the fluid (h_p) is given by E. (25) [32,29]. *Pr* is the Prandtl number given by Eq. (26).

$$h_p = \left(0.37 Re^{0.6} Pr^{0.33} + 0.1\right) \frac{k_f}{d_p} \quad (25)$$

$$Pr = \frac{\mu C_{p,f}}{k_f} \quad (26)$$

The heat transfer between fluid and wall happens at the wall boundary, defined by a constant surface temperature. The fluid-to-wall heat transfer coefficient (h_{fw}) is given by Eq. (27) [33,29]. Here, f_d is the fraction of the contact time of the dense phase with the wall and is given by Eqs. (28) [29]. The dense (h_d) and lean (h_l) phase heat transfer coefficients are given by Eqs. (29) and (30) [33,29]. Re_L and Re_p are Reynolds numbers based on Eulerian cell length and particle size, respectively.

$$h_{fw} = h_l + f_d h_d \quad (27)$$

$$f_d = 1 - exp\left(-10 \frac{\theta_p}{\theta_{cp}}\right) \quad (28)$$

$$h_d = 0.525 Re_p^{0.75} \frac{k_f}{d_p} \quad (29)$$

$$h_l = \left(0.46 \bullet Re_L^{0.5} \bullet Pr^{0.33} + 3.66\right) \frac{k_f}{L} \quad (30)$$

The radiation heat transfer from wall to particles (q_{wp}) is modelled with a near-wall model and is given by Eq. (31) [29]. Here, A_w is the area of the wall, T_w is the temperature of the wall, T_p is the particle temperature, σ is the Stefan-Boltzmann constant, F_{wp} is the view factor between wall and particles (calculated within the software at each instance based on particle volume fraction, diameter, and local geometry), and ε_{wp} is the volume-weighted average particle emissivity, which is given by Eq. (32). ε_p is the volume-averaged particle emissivity, and ε_w is the specified emissivity of the wall.

$$q_{wp} = A_w F_{wp} \varepsilon_{wp} \sigma \left(T_w^4 - T_p^4\right) \quad (31)$$

$$\varepsilon_{wp} = \left(\frac{1}{\varepsilon_p} + \frac{1}{\varepsilon_w} - 1\right)^{-1} \quad (32)$$

Reaction kinetics

The calcination reaction ($CaCO_3 \rightarrow CaO + CO_2$) is the main reaction in the calciner. Calcium silicates (mainly belite) can also form inside the calciner when raw meal is calcined [34]. However, the calcination reaction dominates and can explain the decomposition mechanism of $CaCO_3$ inside the calciner [34], so only the calcination kinetics are included in this study.

The calcination kinetics can be described with a shrinking core model according to which the reaction rate is determined by interrelationships between 1) heat transfer to particles and through the product layer, 2) decomposition of calcite, and 3) diffusion of CO_2 through the product layer [35]. The resistance from heat transfer and CO_2 diffusion through the product layer is usually small for particles in the micrometer scale [36], so the heat transfer to the particle surface and decomposition of calcite may dominate the reaction kinetics. Heat transfer to the particle surface was already discussed in the previous section. The decomposition of calcite is given by Eq. (33) [37]. Here, $dm_{p,j}/dt$ is the decomposition or formation of each component j in the meal, M_j is the molecular mass of the component j, ϑ_j is the stochiometric coefficient of the calcination reaction, p_{co2} is the partial pressure of CO_2 in calciner, $A_{sp,c}$ is the surface area of the calcite particles, and A_{eff} is the excess area fraction coming from voids inside the particles (usually between 1 and 5 [37]). Further, k_D is the rate kinetics and p_{eq} is the equillibrium pressure given by Eqs. (34) and (35) [37].

$$\frac{dm_{p,j}}{dt} = M_j \vartheta_j k_D \left(p_{eq} - p_{co2}\right) A_{eff} A_{sp,c} \quad (33)$$

$$k_D = 1.22 \times 10^{-5} exp\left(\frac{-4026}{T_p}\right) \quad (34)$$

$$p_{eq} = 4.192 \times 10^{12} exp\left(\frac{-20474}{T_p}\right) \quad (35)$$

Materials and experimental method

The CPFD model relies on three physical phenomena to be experimentally validated, 1) hydrodynamics, 2) heat transfer, and 3) reaction kinetics.

The hydrodynamics of the fluidized bed was validated with previous experimental work with a lab-scale fluidized bed operating at ambient conditions [38]. The experiments were conducted with fine and coarse alumina particles with the PSDs shown in Fig. 2.3. Alumina was used for experiments as the density ratio between alumina and ambient air is close to the density ratio of lime and CO_2 at 900 °C. With a similar density ratio, alumina particles in cold conditions become comparable to lime particles in hot conditions. The fine alumina was white in color while the coarse alumina was brown [38]. So, it was possible to visually observe the segregation. An X-ray diffraction (XRD) analysis of coarse alumina revealed the presence of impurities such as Fe_2O_3, which probably gave it the brown color. Fine alumina in contrast had negligible impurities [38].

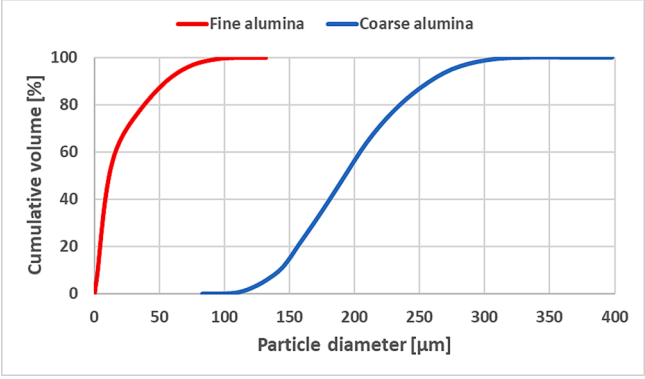

Fig. 2.3. PSD of alumina particles used in experiments.

The experimental setup of the lab-scale fluidized bed rig is shown in Fig. 2.4 (adapted from [38]). The experimental rig comprises an airflow controller, a distributor plate, a vertical tube, and a particle separation system. The flow controller supplies a constant flow rate of air, which passes through the distributor plate to distribute evenly across the vertical tube. Above the distributor, the air meets 2 kg of particles consisting of 25% fine alumina and 75% coarse alumina. The entrained particles can then be collected in a container equipped with a filter through which the gas can escape.

A lab-scale rotary kiln was used to validate both heat transfer and reaction kinetics by calcining raw meal. The hydrodynamics inside the rotary kiln is different from those in the fluidized bed as the powder moves due to the inclination and rotation of the rotary drum. However, the convection and radiation properties of the raw meal powder in contact with the wall should be similar if the hydrodynamics are correct in both designs. Further, raw meal decomposes in both designs, so the reaction kinetics should also be comparable.

The PSDs and composition of the raw meal used for experiments are shown in Fig. 2.2. The experimental setup for the rotary kiln is shown in Fig. 2.5. The rig consists of a rotary tube with three heating zones and one cold zone. The rotary tube is placed inside a heating box, which is heated with silicon carbide heating elements. The raw meal is fed from the cold zone, and each hot zone temperature can be independently controlled. The hot zone end is permanently sealed with an insulation plug. A thermocouple is inserted inside the tube such that its tip is 6 cm away from the insulation plug. A rotameter-controlled stream of N_2/CO_2 can flow through the tube to keep an inert or pure CO_2 environment in the rotary tube.

The experiments are started by feeding 200 g of raw meal into the cold zone. The zone 1 temperature is set at 975 °C, and zones 2 and 3 are set at 650 °C (zones shown in Fig. 2.5), so the system starts to heat up. N_2 is then purged at a high flow rate (400 Nml/min) from the cold zone end to keep the raw meal cool and to remove all the air. After around 2 h, N_2 is replaced with CO_2 at the same flow rate. Once the system is at a pseudo-steady state, the direction of CO_2 is reversed (i.e., gas is now fed from the hot zone end), and the flow rate is reduced to 150 Nml/min. The calciner is tilted to 15° and rotates at 37 RPM. The raw meal travels to zone 1, and the internal thermocouple picks up the particle temperature. The experiments are continued for around 15 mins. After 15 mins, the calciner is inclined back, and the cold-flow lid is opened to get all the particles outside. The remaining particles inside the tube are scraped off with scrapes, and the calcination degree is measured on the collected sample by comparing the loss on ignition (LOI) of the calcined meal against the raw meal.

LOI is measured by first placing the sample at 950 °C for around 5 h in a muffle furnace to release all the CO_2. Then the weight is measured before and the after the test to determine the LOI.

Simulation setup

Three geometries are drawn in SolidWorks, including 1) the cold-flow fluidized bed rig, 2) the hot-flow rotary kiln, and 3) the hot-flow fluidized bed calciner. The number of cells in the mesh for these three geometries are 75174, 58050, and 92840, corresponding to an average cell size of 7, 5, and 95 mm, respectively. The hot-flow fluidized bed calciner was also simulated with a finer mesh of 150,917 cells, and the difference in pressure drop between the coarse and the fine mesh was lower than 5%. The chosen cell size was seen as acceptable, and the results are mesh independent. The meshed geometries are shown in Fig. 2.6.

The simulation time step was controlled with the Courant–Friedrichs–Lewy (CFL) number, which was set between 0.8 and 1.5, as

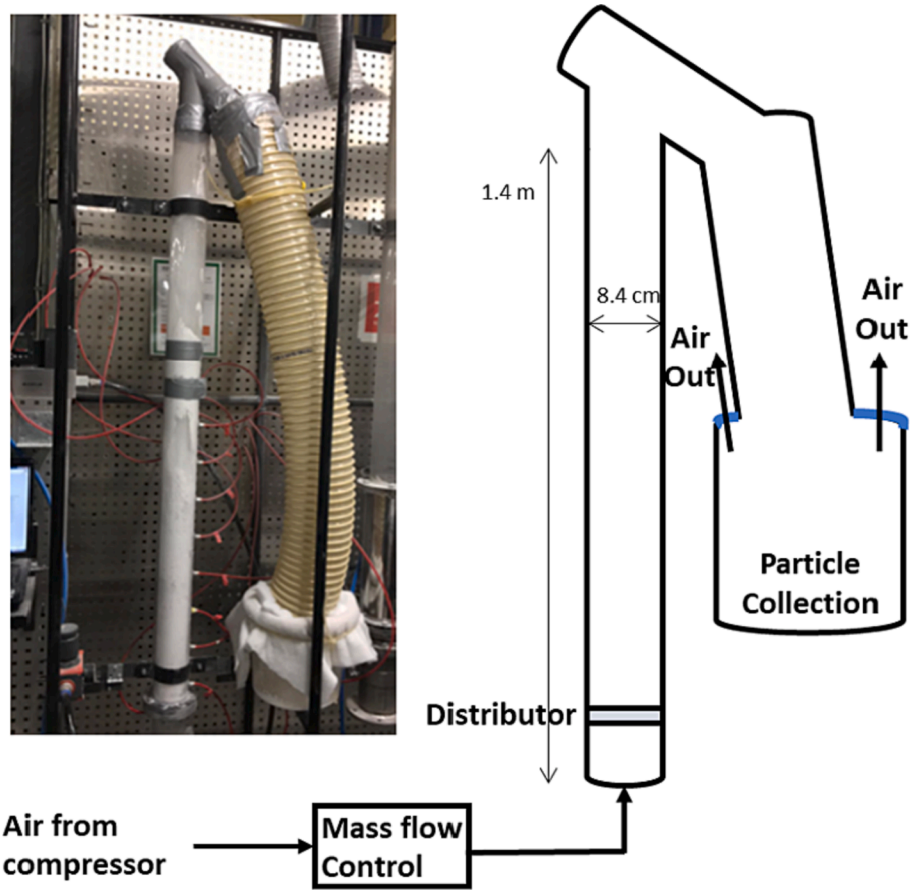

Fig. 2.4. Experimental setup of lab-scale fluidized bed rig (adapted from [38]).

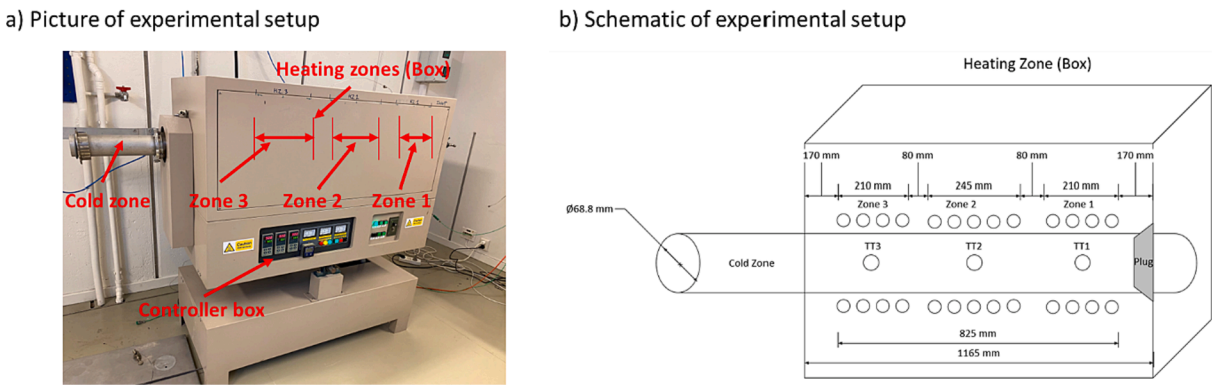

Fig. 2.5. Experimental rig for rotary kiln.

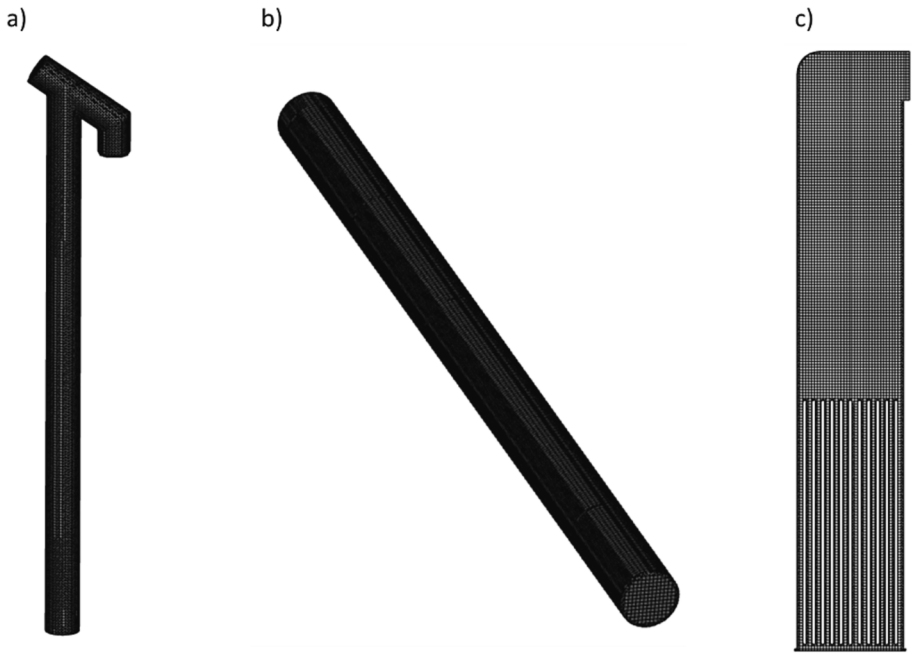

Fig. 2.6. Meshing for a) cold-flow fluidized bed, b) rotary kiln, c) fluidized bed calciner.

recommended by the user manual [29]. All the simulations were conducted until a pseudo-steady state was achieved. The time-averaged results were obtained by averaging the spacial results at an interval of 2 s in the pseudo-steady state region of the simulation.

The cold-flow fluidized bed calciner has cold air entering from the bottom boundary and leaving from the outlet boundary at the top. Simulations are conducted at an isothermal temperature of 300 K. The rotary calciner has a constant temperature boundary condition in each of the three wall zones, and the temperature value is the same as in the experiments. The CO_2 produced from the calcination reaction exits from the cold outlet end of the rotary tube. The rotation and inclination effect of the rotary kiln was simulated by rotating the gravitational boundary conditions. The rotary kiln was rotated at 37 RPM and inclined at 15°, similar to experimental conditions.

The fluidized bed calciner has CO_2 entering at the bottom boundary at 912 °C. The vertical sections in the rig (heaters) are kept at a constant temperature of 1100 °C. The calciner is initially filled with 13562 kg of coarse lime particles. The raw meal is fed from three locations, as shown in Fig. 2.1. Some CO_2 is also fed with the raw meal to assist the feeding. The flow rates, inlet mass fluxes, and inlet temperature of raw meal and CO_2 are shown in Table 2.1.

Table 2.1
Inlet boundary conditions of raw meal, conveying gas, and fluidizing gas for fluidized bed calciner.

Stream	Mass flow rate [t/h]	Inlet mass flux [kg/(m^{2}s)]	Temperature [°C]
Raw meal inlet	10—20	173—416	750
Conveying CO_2 for raw meal	0.120	2.1	750
Fluidizing CO_2 from bottom	0.728	0.06	912

Results and discussions

Model validation

The model is first validated at cold-flow conditions in the fluidized bed. Experimental results showed that good mixing was achieved at a superficial air velocity of around 0.18 m/s, and there was negligible particle entrainment. The air velocity was increased to 0.9 m/s, where 94% of fine particles were entrained. The segregation was confirmed visually as the fine particles were white while the coarse particles were dark brown.

The simulations were conducted with the Wen-Yu drag model for fine alumina and the blended Ergun and Wen-Yu model for coarse alumina particles. The results showed negligible fine or coarse particle entrainment at 0.18 m/s. The entrainment was observed at 0.9 m/s, where 93% of the initial 0.5 kg of fine alumina was entrained from the bed (see Fig. 3.1). So, the hydrodynamics was successfully validated, and the model could be used for further simulations.

The heat transfer and reaction kinetics were then validated at the rotary kiln hot-flow conditions. During the experiments, a calcination degree of 69 % was achieved within 850 s. The particle temperature was continuously measured during the experiments.

Initial simulations were conducted with the Wen-Yu drag model for raw meal. However, the raw meal started to fluidize in the simulations due to CO_2 produced from the calcination reaction. This revealed that the chosen drag model was not appropriate for rotary kiln simulations with raw meal particles. The raw meal particles are cohesive and stick to the wall when present as bulk particles. This phenomenon was simulated by reducing the drag predictions from the CPFD model by multiplying the predicted drag with a small number of 0.01. A comparison of the predicted particle temperature and calcination degree from the CPFD simulations and the experimentally measured values are shown in Fig. 3.2. The particle temperature from the CPFD simulations is taken from the region of the thermocouple, and the calcination degree is taken by accounting for all the particles, to be consistent with the experimental results. The match between the two temperature profiles is very good. The final calcination degree from simulations was predicted to be 68%, close to the experimental calcination degree. So, the heat transfer and reaction kinetics were successfully validated. The validated hydrodynamics, heat transfer, and reaction kinetics model made it possible to simulate the fluidized bed calciner with acceptable accuracy.

Simulation of fluidized bed calciner

The fluidized bed calciner was simulated using the validated drag model from the cold-flow fluidized bed and the heat transfer and reaction kinetics model from the hot-flow rotary kiln. The raw meal feeding was increased from 10 to 24 t/h in steps until a pseudo-steady state was achieved at each flow rate. A comparison of the inlet flow rate of raw meal, the outlet flow rate of the calcined meal, and the outlet flow rate of coarse lime are shown in Fig. 3.3. Further, the steady-state calcination degree and CO_2 production at different feeding rates are shown in Fig. 3.4.

The outlet flow rate of the calcined meal and coarse lime fluctuates as the system is not perfectly mixed. Due to imperfect mixing, some particles stay longer inside the bed than others which causes the mass flow rate to either overshoot or undershoot at a particular instance. The fluctuations are high as particle flow tends to be more heterogenous when compared to fluid flow. The average of the fluctuations at each raw meal feed level is also shown in Fig. 3.3.

The mass flow rate of the calcined meal is lower than the raw meal feeding rate due to the mass lost from CO_2 released in the calcination reaction. The results show negligible coarse entrainment at a feeding rate of raw meal between 10 and 16 t/h. The entrainment of coarse particles at a low flow rate of 0.1 t/h started from the raw meal feeding of 16 t/h. The entrainment depends on gas velocity inside the calciner, which is dependent on the gas flow rate. As the inlet gas flow rate is constant, the gas flow rate is mainly affected by the CO_2 production rate. The production rate of CO_2 depends on two factors: 1) Calcination degree: At a higher calcination degree, more $CaCO_3$ is getting converted to CO_2, thereby increasing the gas production, 2) Mass flow rate of raw meal: At a higher mass flow rate of raw meal ($CaCO_3$), an identical calcination degree will produce more CO_2. The calcination degree dropped with increasing particle flow rate due to insufficient heat transfer. However, the CO_2 production kept increasing due to the dominance of the second factor (higher mass flow rate of raw meal). Increasing the raw meal feeding from 22 to 24 t/h decreased the CO_2 production rate because the first factor (lower calcination degree) dominated. The gas flow rate at 24 t/h is still higher than at 16 t/h, increasing the entrainment of coarse particles to around 0.7 t/h.

The calcination degree was reduced below 90% at a feeding rate higher than 16 t/h. In a commercial calciner, it is desired to have a calcination degree higher than 90% [14]. So, the designed calciner can be operated within the raw meal feeding range from 10 to 16 t/h. At these feeding rates, a pure CO_2 of around 0.33 kg-CO_2/kg-raw-meal could be produced. Further, the design needs between 0.05 and 0.09 kg-CO_2/kg-raw-meal from the bottom as recycled gas.

The front view of time-averaged pressure drop and bulk density of particles in the Eulerian cells at a raw meal feeding rate of 14 t/h is shown in Fig. 3.5. Property variation along the calciner height is also shown as an x-y plot by averaging in the other two directions.

The total pressure drop inside the calciner is around 520 mbar. The bulk of the particles lies below the calciner height of 6 m, and this region contains most of the pressure drop. So, the pressure drop mainly comes from the particle weight. The pressure drop across the calciner limits the maximum bed height. The bed height could be further increased if a higher pressure drop is acceptable in the system.

The time-averaged gas velocity profile inside the calciner is shown in Fig. 3.6. The 3-D plot of the velocity profile is shown at three different

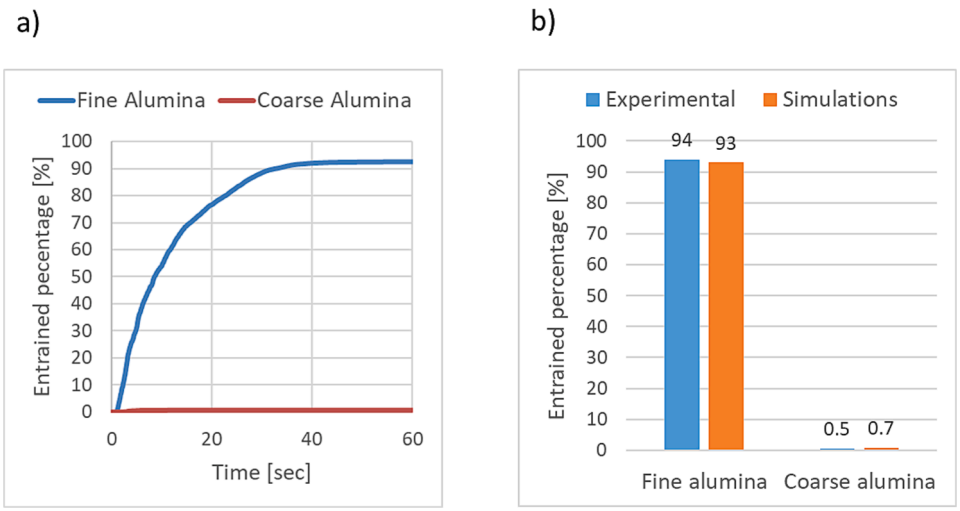

Fig. 3.1. Entrainment of fine alumina at a superficial gas velocity of 0.9 m/s, a) transient entrainment during simulations, b) comparison of final entrainment in experiments and simulations.

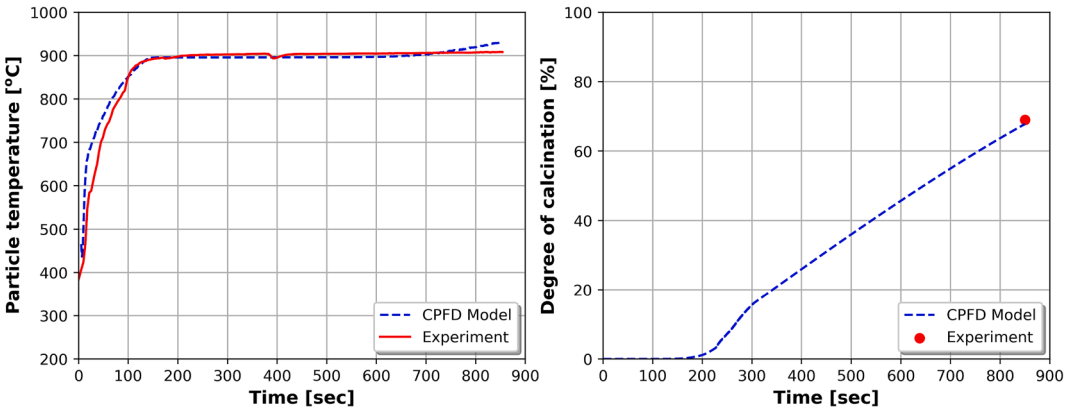

Fig. 3.2. Predicted particle temperature and calcination degree from CPFD model and experiments.

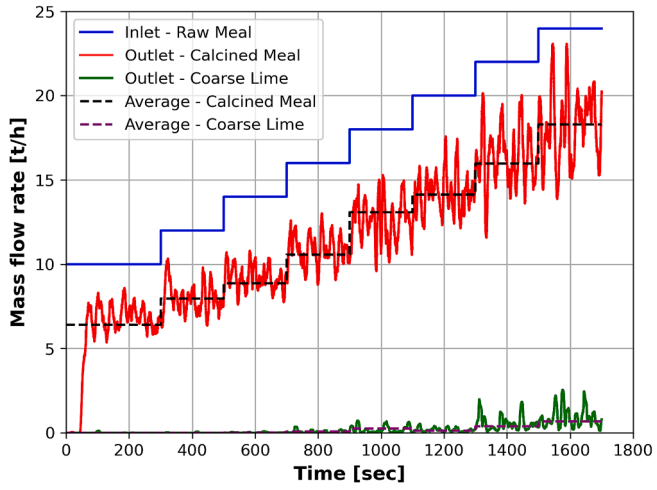

Fig. 3.3. Inlet and outlet flow rate of particles from the calciner during the simulations.

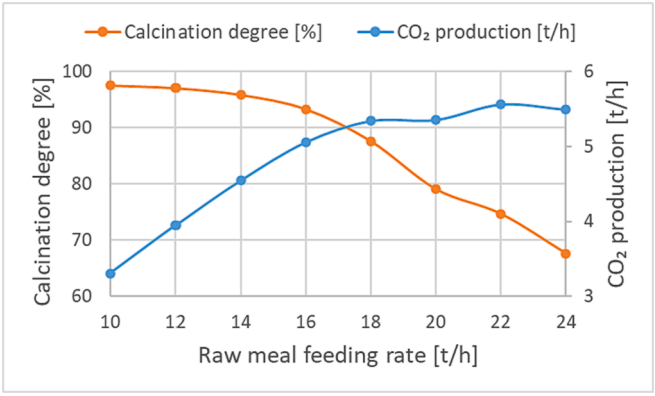

Fig. 3.4. Steady-state calcination degree and CO_2 production from the reaction predicted at different raw meal feeding rates.

depths in the calciner (i.e., front, middle, and back) at a raw meal feeding of 14 t/h. Further, the gas velocity profile along the calciner height at different raw meal feeding rates is also shown by averaging the velocity in length and depth directions.

The gas velocity in the bed steadily increased along the height due to higher production of CO_2 with the calciner height. A deceleration zone above the mixing chamber is due to a wider cross-section. The gas velocity almost flattens out in the segregation region, indicating a smooth operation of the calciner. High-velocity zones are observed at three regions of the mixing chamber, more specifically, where the raw meal is fed. This is due to the high CO_2 production in these regions. Improving the meal distribution further could reduce the velocity surge. However, with the current setup, the calciner can be operated with a relatively smooth velocity profile in the segregation region.

The gas velocity at the top of the calciner is the most important parameter for good segregation. The raw meal feeding of 10 t/h produces a gas velocity of around 1 m/s. The velocity increases to around 1.3 m/s by increasing the feeding rate of raw meal to 16 t/h. The gas production rate at the raw meal feeding rate of 16 t/h to 24 t/h is not significantly affected (see Fig. 3.4), so the velocities are similar for these conditions. Thus, to have a good segregation, the gas velocity at the top of the calciner should be 1.0 to 1.3 m/s. It is possible to operate at lower velocities, but then the segregation rate may not be high enough, and particles may start to accumulate.

The average raw meal temperature, residence time, particle size, and calcination degree inside the calciner at a raw meal feeding rate of 14 t/h are all shown in Fig. 3.7.

The results show that the raw meal exits at around 912 °C from the calciner. The particle temperature in the mixing chamber is between 950 and 1000 °C. This is because the bigger raw meal particles tend to stay longer in the bed, as seen from the residence time and particle size results. The particles are already calcined within the bed height as the heat is transferred in this region. The average particle size of exiting particles is around 22 μm, which is also the average size of the raw meal particles. Overall the results are promising, and it would be interesting to run hot-flow experiments with such an electrified calciner design.

Conclusions

This work demonstrated a design of an electrified fluidized bed raw meal calciner operating with binary particles, potentially requiring a low gas feeding from the bottom of the calciner. A CPFD model of the calciner was used to simulate the calciner. The CPFD model was validated for hydrodynamics, heat transfer, and reaction kinetics by means of experimental results. The hydrodynamics was first validated by comparing the results against a cold-flow fluidized bed rig. The heat transfer and reaction kinetics were then validated with a hot-flow experimental rotary kiln. The simulated results were all found to be close to the experimental results, so the model was considered successfully validated.

The validated CPFD model was used to simulate a pilot-scale fluidized bed calciner, and the results indicated that a feed rate between 10 and 16 t/h gave good operational values. At these conditions, the calcination degree was above 90%, and the entrainment of coarse particles was negligible. Further, the calcination reaction could produce a pure CO_2 of around 0.33 kg-CO_2/kg-raw-meal, and a gas recycling from

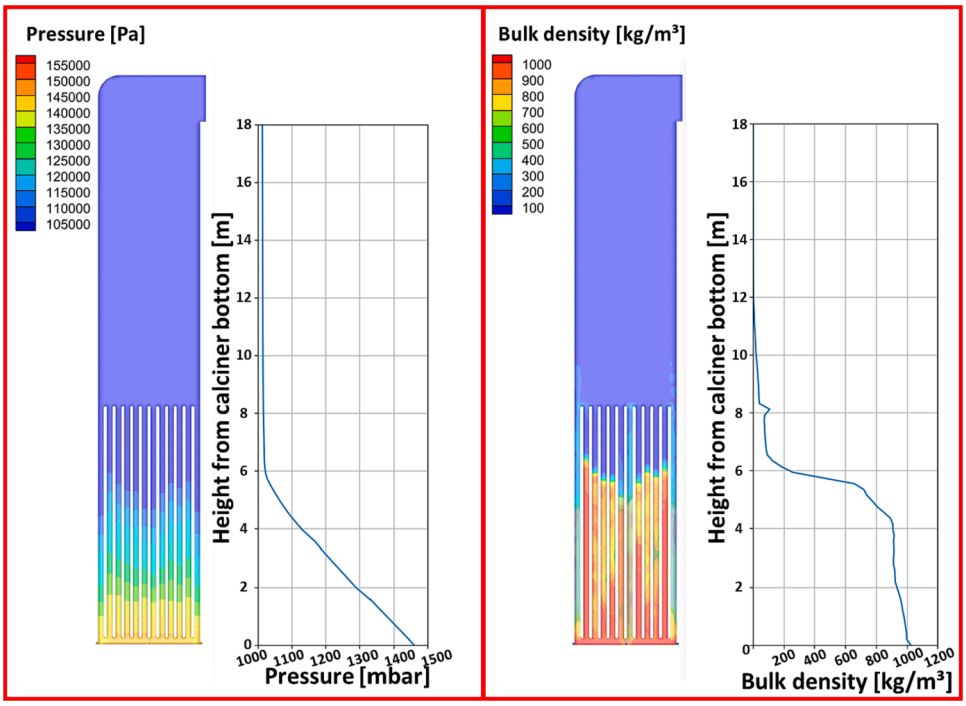

Fig. 3.5. Time-averaged front view of pressure drop and bulk density at raw meal feeding of 14 t/h.

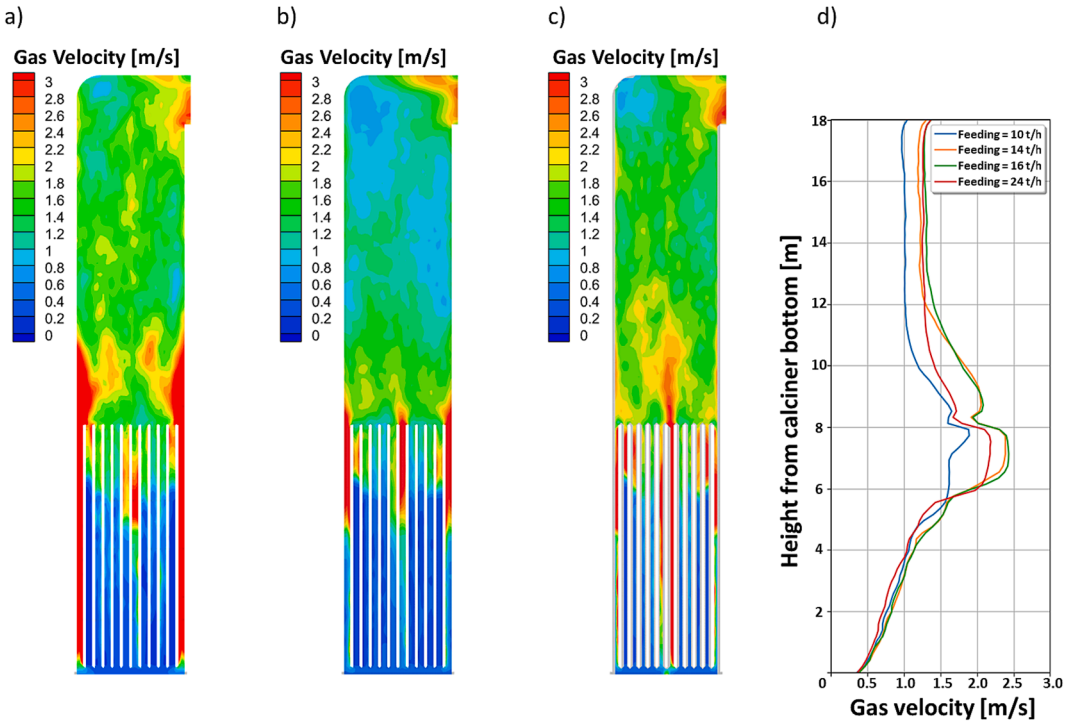

Fig. 3.6. Time-averaged gas velocity [m/s] profile inside the calciner. a) front contour at a feeding rate of 14 t/h, b) middle contour at a feeding rate of 14 t/h, c) back contour at a feeding rate of 14 t/h, and d) space averaged velocity profile along the calciner height at a feeding rate of 10, 14, 16 and 24 t/h.

0.05 to 0.09 kg-CO_2/kg-raw-meal was required.

The calciner performance was analyzed with time and space-averaged results inside the calciner. The total pressure drop was around 520 mbar, most of which lay within the bulk particles with a bed height of 6 m. So, the contribution of bed weight to the pressure drop was higher than the frictional losses from the gas flow. Increasing the bed height would also increase the pressure drop, and the maximum bed height is limited based on the acceptable level of pressure drop. Gas velocities between 1.0 and 1.3 m/s gave negligible entrainment of coarse particles, and these velocities were generated at the raw meal feeding between 10 and 16 t/h. The average gas velocity along the height was almost constant in the segregation chamber, and a smooth operation was achieved. The raw meal temperature at the exit was around 912 °C, and the average size of the exiting particles was close to

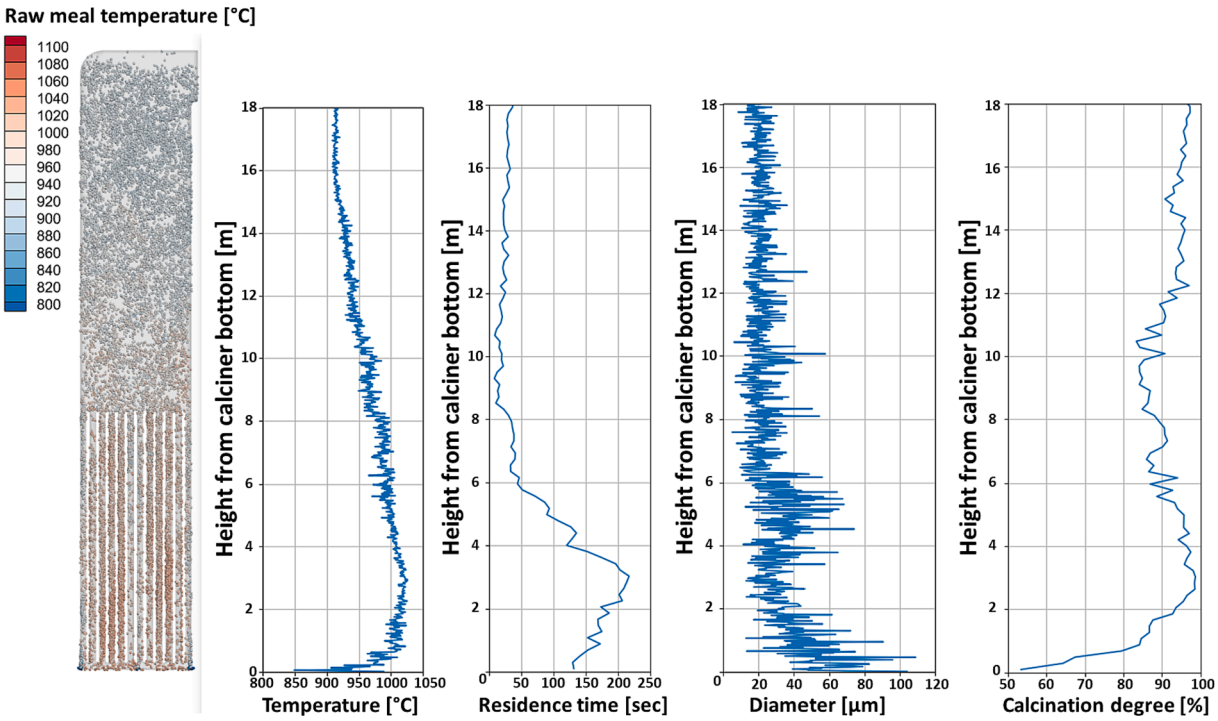

Fig. 3.7. Raw meal temperature, residence time, diameter, and calcination degree with a feeding rate of 14 t/h.

the original raw meal size.

The simulation results are promising, and such a calciner can likely be used for electrification in the cement industry. However, the concept has only been tested with simulations validated by experiments under other conditions, so conducting experiments with the suggested design in the future is recommended.

CRediT authorship contribution statement

Ron M. Jacob: Conceptualization, Methodology, Software, Validation, Investigation, Writing – original draft, Visualization. **Lars-André Tokheim:** Conceptualization, Methodology, Validation, Investigation, Writing – review & editing, Visualization, Supervision, Project administration, Funding acquisition.

Declaration of Competing Interest

The authors declare that they have no known competing financial interests or personal relationships that could have appeared to influence the work reported in this paper.

Data availability

Data will be made available on request.

Acknowledgment

This study was done as part of the Norwegian research project “ELSE 2” which is short (in Norwegian) for “electrified cement production, part 2”. The project has several partners in addition to USN, including Norcem, Cementa, Kanthal and Sintef. They are all acknowledged for their suggestions and collaboration. The project was funded by Norcem AS and CLIMIT (a Norwegian research programme, project number 620035), so they are also greatly acknowledged. The authors are grateful to Arvid Stjernberg and Christoffer Moen from Heidelberg Materials (parent company of Norcem and Cementa) for reading and giving useful comments to the article.

References

[1] IEA. Industry. https://www.iea.org/reports/industry; 2022 [accessed 16 January 2023].
[2] IEA. Technology Roadmap: Low-carbon transition in the cement industry. https://www.iea.org/reports/technology-roadmap-low-carbon-transition-in-the-cement-industry; 2018 [accessed 30 March 2023].
[3] H F W Taylor. Cement Chemistry. Academic Press. 1990.
[4] Nakhaei M, Grévain D, Jensen LS, Glarborg P, Johansen KD, Wu H. NO emission from cement calciners firing coal and petcoke: a CPFD study. Applications in Energy and Combustion Science 2021;5:100023. https://doi.org/10.1016/j.jaecs.2021.100023.
[5] Bjerge LM, Brevik P. CO2 capture in the cement industry, norcem CO2 capture project (Norway). Energy Procedia 2014;63:6455–63. https://doi.org/10.1016/j.egypro.2014.11.680.
[6] Aromada SA, Eldrup NH, Øi LE. Capital cost estimation of CO2 capture plant using enhanced detailed factor (EDF) method: installation factors and plant construction. Int J Greenhouse Gas Control 2021;110:13394. https://doi.org/10.1016/j.ijggc.2021.103394.
[7] Kim S, Lim Y-I, Lee D, Cho W, Seo MW, Lee JG, et al. Perspectives of oxy-coal power plants equipped with CO2 capture, utilization, and storage in terms of energy, economic, and environmental impacts. Energ Conver Manage 2022;273:116361.
[8] Hills T, Leeson D, Florin N, Fennell P. Carbon capture in cement industry: technologies, progress and retrofitting. Environ Sci Tech 2016;50:368–77. https://doi.org/10.1021/acs.est.5b03508.
[9] Reitz M, Junk M, Ströhle J, Epple B. Design and operation of a 300 kWth indirectly heated carbonate looping pilot plant. Int Jof Greenhouse Gas Control 2016;54:272–81. https://doi.org/10.1016/j.ijggc.2016.09.016. Part 1.
[10] Kanellis G, Zeneli M, Nikolopoulos N, Hofmann C, Ströhle J, Karellas S, et al. CFD modelling of an indirectly heated calciner reactor, utilized for CO2 capture, in an Eulerian framework. Fuel 2023;346:128251. https://doi.org/10.1016/j.fuel.2023.128251.
[11] Hills TP, Sceats M, Rennie D, Fennell P. LEILAC: Low cost CO2 capture for the cement and lime industries. Energy Procedia 2017;114:6166–70. https://doi.org/10.1016/j.egypro.2017.03.1753.
[12] CORDIS. Low Emissions Intensity Lime and Cement 2: Demonstration Scale. https://cordis.europa.eu/project/id/884170; 2021 [accessed 5 March 2023].
[13] Tokheim LA, Mathisen A, Øi LE, Jayarathna C, Eldrup N, Gautestad T. Combined calcination and CO2 capture in cement clinker production by use of electrical energy. SINTEF Proceedings (TCCS-10) 2019;4:101–9.
[14] Jacob RM, Tokheim LA. Electrified calciner concept for CO2 capture in pyro-processing of a dry process cement plant. Energy 2023;268:126673. https://doi.org/10.1016/j.energy.2023.126673.
[15] Jacob RM, Tokheim LA. Electrification of an Entrainment Calciner in a Cement Kiln System – Heat Transfer Modelling and Simulations. In: Linköping Electronic Conference Proceedings (62nd SIMS, September 21st-23rd, virtual conference); 2021. https://doi.org/10.3384/ecp2118567.

[16] Jacob RM, Tokheim LA. Novel design of a rotary calciner internally heated with electrical axial heaters: experiments and modelling. Results in Engineering 2023; 17:100992. https://doi.org/10.1016/j.rineng.2023.100992.
[17] Kunii D, Levenspiel O. Fluidization engineering. Butterworth-Heinemann, 2nd Edition 1991.
[18] Erans M, Nabavi SA, Manović V. Pilot-scale calcination of limestone in steam-rich gas for direct air capture. Energy Conversion and Management: X 2019;1:100007. https://doi.org/10.1016/j.ecmx.2019.100007.
[19] R M Jacob, B M Moldestad, L A Tokheim. Fluidization of Fine Calciner Raw Meal Particles by mixing with coarser Inert Particles – Experiments and CPFD Simulations. Linköping Electronic Conference Proceedings (62nd SIMS, September 21st-23rd, virtual conference). 2021. https://doi.org/10.3384/ecp21185333.
[20] Geldart D. Types of gas fluidization. Powder Technol 1973;7:285–92. https://doi.org/10.1016/0032-5910(73)80037-3.
[21] Kato K, Takarada T, Matsuo N, Suto T, Nakagawa N. Residence time distribution of fine particles in a powder-particle fluidized bed. Kagaku Kogaku Ronbunshu 1991; 17(5):970–5.
[22] Tashimo T, Suto T, Murota J, Kato K. Calcination of fine limestone particles by a powder-particle fluidized bed. J Chem Eng Jpn 1999;32:374–8. https://doi.org/10.1252/jcej.32.374.
[23] Andrews MJ, O'Rourke PJ. The multiphase particle-in-cell (MP-PIC) method for dense particulate flows. Int J Multiph Flow 1996;22:379–402. https://doi.org/10.1016/0301-9322(95)00072-0.
[24] Snider DM. An incompressible three-dimensional multiphase particle-in-cell model for dense particle flows. J Comput Phys 2001;170:523–49. https://doi.org/10.1006/jcph.2001.6747.
[25] Snider DM, Clark SM, O'Rourke PJ. Eulerian-Lagrangian method for three-dimensional thermal reacting flow with application to coal gasifiers. Chem Eng Sci 2011;66:1285–95. https://doi.org/10.1016/j.ces.2010.12.042.
[26] Green DW. R H Perry. Perry's Chemical Engineering Handbook: McGraw-Hill; 2008.
[27] Smagorinsky J. General circulation experiments with the primitive equations: I. The Basic Experiment Monthly Weather Review 1963;91:99–164. https://doi.org/10.1175/1520-0493(1963)091<0099:GCEWTP>2.3.CO;2.
[28] O'Rourke PJ, Snider DM. A new blended acceleration model for the particle contact forces induced by an interstitial fluid in dense particle/fluid flows. Powder Technol 2014;256:39–51. https://doi.org/10.1016/j.powtec.2014.01.084.
[29] Barracuda BC. Virtual Reactor User Manual 2023.
[30] Beetstra R, Van Der Hoef MA, Kuipers JAM. Drag force of intermediate Reynolds number flow past mono- and bidisperse arrays of spheres. AIChE J 2007;53: 489–501. https://doi.org/10.1002/aic.11065.
[31] Wen CY, Yu YH. Mechanics of fluidization. Chemical Engineering Progress Symposium 1966:100–11.
[32] Fan L-S, Zhu C, editors. Principles of Gas-Solid Flows. Cambridge University Press; 1998.
[33] Yang WC. Handbook of fluidization: fluid-particle systems. Taylor & Francis Group 2003.
[34] Fernandez JR, Turrado S, Abanades JC. Calcination kinetics of cement raw meals under various CO2 concentrations. React Chem Eng 2019;4:2129–40. https://doi.org/10.1039/C9RE00361D.
[35] Satterfield CN, Feakes F. Kinetics of the thermal decomposition of calcium carbonate. AIChE J 1959;5:115–22. https://doi.org/10.1002/aic.690050124.
[36] Borgwardt RH. Calcination kinetics and surface area of dispersed limestone particles. AIChE J 1985;31:103–11. https://doi.org/10.1002/aic.690310112.
[37] Mikulčić H, Berg EV, Vujanović M, Priesching P, Perković L, Tatschl R, et al. Numerical modelling of calcination reaction mechanism for cement production. Chem Eng Sci 2012;69:607–15. https://doi.org/10.1016/j.ces.2011.11.024.
[38] Kanabi L, Kumarawela TR, Alex JS. Electrified calcination combined with CO2 capture in a fluidized bed calciner - Fluidization of scaled binary particles. Project: University of South-Eastern Norway; 2022.